

Tunable Graphene Metasurfaces with Gradient Features by Self-Assembly-Based Moiré Nanosphere Lithography

Zilong Wu, Wei Li, Maruthi Nagavalli Yogeesh, Seungyong Jung, Alvin Lynghi Lee, Kyle McNicholas, Andrew Briggs, Seth R. Bank, Mikhail A. Belkin, Deji Akinwande,* and Yuebing Zheng*

Patterned arrays of graphene nanostructures, also referred as graphene metasurfaces, have proven to be capable of efficiently coupling with incident light by surface plasmon resonances. In this work, a new type of graphene metasurfaces with moiré patterns using cost-effective and scalable moiré nanosphere lithography (MNSL) is demonstrated. A large gradient in feature size (i.e., from sub-200 nm to 1.1 μm) of the graphene nanostructures exists in single metasurfaces. The in-plane quasi-periodic arrangement of the graphene nanostructures can be easily tuned to form a variety of moiré patterns. The experimental measurement and numerical simulations show that the graphene moiré metasurfaces support tunable and multiband optical responses due to the size and shape dependences of surface plasmon resonance modes of graphene nanostructures. It is also demonstrated that the multiband optical responses of graphene moiré metasurfaces can be tuned from mid-infrared (MIR) to terahertz (THz) regimes by choosing polystyrene spheres of different sizes for MNSL. These findings provide a cost-effective and scalable strategy to achieve ultrathin functional devices, including multiband light modulators, broadband biosensors, and multiband photodetectors, which feature tunable and multiband responses in wide range of wavelengths from MIR to THz.

surface plasmon polaritons supported by graphene have shown great potentials for enhanced nanophotonic and optoelectronic applications due to strong mode confinement and tunable resonance peak wavelength via electrostatic and chemical doping.^[2,9–16] Recent studies have shown that graphene metasurfaces, made of periodic arrays of graphene nanostructures that support surface plasmons, are promising candidates for biosensing with superior sensitivity than their metal counterparts.^[17,18] The enhanced light-matter interactions from plasmonic effects of the graphene nanostructures have also been applied to build light modulators with improved signal-to-noise ratio, sensitivity, and modulation depth.^[19]

Optical metasurfaces are 2D arrangements of subwavelength structures, which can manipulate the electromagnetic waves in a specifically designed way. Compared with their 3D counterparts known as metamaterials, metasurfaces features the

advantages of ultrathin structures and potential for simple fabrication. Recent years have witnessed tremendous success in developing metasurfaces consisted of plasmonic nanostructures as building blocks, which have shown promise for a variety of applications, including light beam manipulation,^[20] polarization control,^[21,22] and light absorption and filtering.^[23] In particular, plasmonic metasurfaces with multiband responses have attracted strong interests in further enhancing the applications. For example, their resonance peaks can be matched with both resonant Raman frequencies and infrared vibrational frequencies of molecules to produce substrates for simultaneous surface-enhanced Raman spectroscopy (SERS) and surface-enhanced infrared spectroscopy (SEIRS).^[24–29] Multiband metasurfaces have also been applied to enhance the signals from multiple infrared vibrational modes of biomolecules to achieve precise discriminators for different species by detecting multiple vibrational fingerprints.^[25–27,30] Besides molecule sensing, multiband devices at various electromagnetic spectral bands are also highly desired to meet the strong demand for the ever-increasing accuracy and high speed in surveillance and communication systems.^[31–33] In conventional metallic plasmonic metasurfaces, the multiband responses have been achieved by designing patterns with

1. Introduction

Graphene, one of the most exciting 2D materials, has attracted strong interests due to its extraordinary mechanical, thermal, optical, electronic, and magneto-optical properties.^[1–8] Recently,

Z. Wu, W. Li, Prof. Y. Zheng
Department of Mechanical Engineering
Materials Science and Engineering Program
and Texas Materials Institute
The University of Texas at Austin
Austin, TX 78712, USA
E-mail: zheng@austin.utexas.edu

W. Li, M. N. Yogeesh, Dr. S. Jung, A. L. Lee, K. McNicholas,
A. Briggs, Prof. S. R. Bank, Prof. M. A. Belkin, Prof. D. Akinwande
Microelectronics Research Centre
The University of Texas at Austin
Austin, TX 78758, USA
E-mail: deji@ece.utexas.edu

Dr. S. Jung, Prof. M. A. Belkin
Department of Electrical and Computer Engineering
The University of Texas at Austin
Austin, TX 78712, USA



DOI: 10.1002/adom.201600242

complex structures,^[27,34] quasiperiodic arrangements,^[35] or gradient components.^[24,36]

Applications, such as SERS and SEIRS, as well as multispectral plasmon infrared biosensors, require multispectral metasurfaces tailored for operation at application-specific bands. Easy-to-fabricate multiband metasurfaces with controllable resonance positions are highly desired for these applications. Plasmonic metasurfaces with moiré patterns show great potentials to meet the requirements in multiband and tunability. It has been reported that plasmonic nanostructures arranged in quasiperiodic lattices exhibit an increased number of resonance bands compared with their periodic counterparts.^[35,37] Also, the large amount of nanostructures with gradient in shape and size in metasurfaces with moiré patterns can further contribute to the multiband properties. Besides multiband properties, moiré metasurfaces fabricated by moiré nanosphere lithography are also featured by their tunability in the number and wavelength of resonance bands.^[24,38] Au metasurfaces with moiré patterns have been reported to exhibit multiple resonance bands from visible to near-infrared to mid-infrared (MIR) regimes, which can be applied, e.g., for simultaneously enhancing Raman signals and infrared vibrational signals of biomolecules to improve the sensitivity and accuracy of biosensing. The moiré metasurfaces are also expected to be suitable for multiband THz devices and multiband radar systems in defense platforms if one can further tune the resonance bands to the longer wavelength.^[32,39]

Herein, we have developed an effective approach to pattern large-area graphene layer, which is grown by chemical vapor deposition (CVD), into moiré metasurfaces. The metasurfaces feature moiré patterns with high quasiperiodicity and gradient components, which lead to unique properties as shown by both experimental and theoretical studies. Graphene sheets with an atomic-scale moiré superlattice, produced by the superposition of two layers with hexagonal patterns, have been reported to show unique optical and electronic properties including gate-dependent pseudospin mixing,^[40] novel plasmonic modes,^[41] and localization of Dirac electrons.^[42] With MNSL, we extend the family of graphene surfaces with moiré patterns to nano and micrometer scales, leading to graphene moiré metasurfaces that exhibit controllable, quasiperiodic, and gradient nanostructures with feature sizes from sub-200 nm to 1.1 μm . Further decrease of feature size down to sub-60 nm could be achieved by using nanospheres with size of 60 nm for MNSL. Measured and simulated results illustrate that multiple IR plasmon resonances can be excited in these graphene metasurfaces due to the shape and size dependences of the plasmon resonance modes of the graphene nanostructures. The plasmonic resonances can also be spectrally tuned by controlling the patterns of the graphene metasurfaces, which can be achieved by changing the in-plane relative rotation angle between the two nanosphere monolayers in the MNSL. We further demonstrate that the resonance peaks of the graphene metasurfaces can be tuned from MIR ($\lambda \approx 3\text{--}30 \mu\text{m}$) to terahertz (THz, $\lambda \approx 30\text{--}1000 \mu\text{m}$ or 10 to 0.3 THz) regime through choosing polystyrene (PS) nanospheres of different sizes for MNSL. Our study has expanded the family of graphene metasurfaces and offered a cost-effective and scalable strategy to achieve ultrathin functional devices with tunable and multiband responses.

2. Results and Discussion

Metasurfaces consisted of graphene nanodisk arrays were achieved by combining nanosphere lithography and reactive ion etching (RIE).^[43] The size of graphene nanodisks were adjusted by controlling the RIE time. Herein, the graphene is patterned into moiré metasurfaces using MNSL^[24,38] with O₂ RIE for variable times.^[44] The CVD-grown graphene is first transferred to double-side polished high-resistivity Si substrates by a poly(methyl methacrylate) (PMMA)-assisted wet transfer process.^[45,46] Two monolayers of PS nanospheres with diameter of 500 nm are then subsequently deposited on the graphene,^[24,38] as shown in **Figure 1a**. In brief, colloidal PS nanospheres are self-assembled into monolayer at the water–air interface and then transferred to the substrates with graphene after evacuating the water. A second monolayer of PS nanospheres is then deposited on top of the first PS monolayer via a similar process. The relative in-plane rotation angle between the first and the second PS monolayer can be controlled to obtain various moiré patterns. Then, RIE with O₂ plasma is applied to reduce the size of the PS nanospheres to create voids between the closely packed nanospheres. The graphene in the voids is then exposed to O₂ plasma and etched away. This process is followed by ultrasonication in toluene for 5 min to remove the PS nanospheres, leaving graphene sheets that are patterned into the moiré metasurfaces. **Figure 1b** shows the scanning electron microscopy (SEM) image of a typical graphene moiré metasurfaces, where the dark and bright parts are graphene and exposed Si substrates, respectively. Complex graphene nanostructures with high reproducibility and good quasiperiodicity are obtained. Due to the relative rotation angle between the top and the bottom PS nanosphere monolayers, large area graphene quasiperiodic lattices with high rotational order, and the sixfold rotational symmetry can be achieved. The Raman spectra of as transferred graphene show a negligible defect peak and a high peak intensities at 2D (2690 cm^{-1}) and G (1580 cm^{-1}) band. As the defect scattering in graphene increases after patterning, the Raman intensity increases for two separate disorder peaks,^[47,48] D (1350 cm^{-1}) and D' (1620 cm^{-1}), presented in **Figure 1c**. We demonstrate that the quality of the graphene is uniform in a large area by characterizing the Raman spectra of ten different locations of the sample with graphene moiré metasurfaces (**Figure S1**, Supporting Information), where the locations are separated by at least 100 μm from each other.

In contrast to the conventional nanosphere lithography that applies only one monolayer of PS nanospheres as etching mask and can achieve limited types of regular structures such as nanodisks and nanotriangle antidots,^[49] the patterns resulting from the two-layer PS nanosphere mask with various relative in-plane rotation angle are much more complex. **Figure 2** demonstrates the capability of constructing various graphene moiré metasurfaces with this method. **Figure 2a–c** schematically show stacking of two PS nanosphere monolayers with different relative in-plane rotation angles. The relative rotation angles are 7.5°, 12°, and 19° from **Figure 2a–c**, respectively. All patterns are characterized by moiré lattices with high rotational symmetry without translational symmetry. However, the size of the unit cell and the quasiperiodicity of the patterns decrease with increasing relative in-plane rotation angle. In addition,

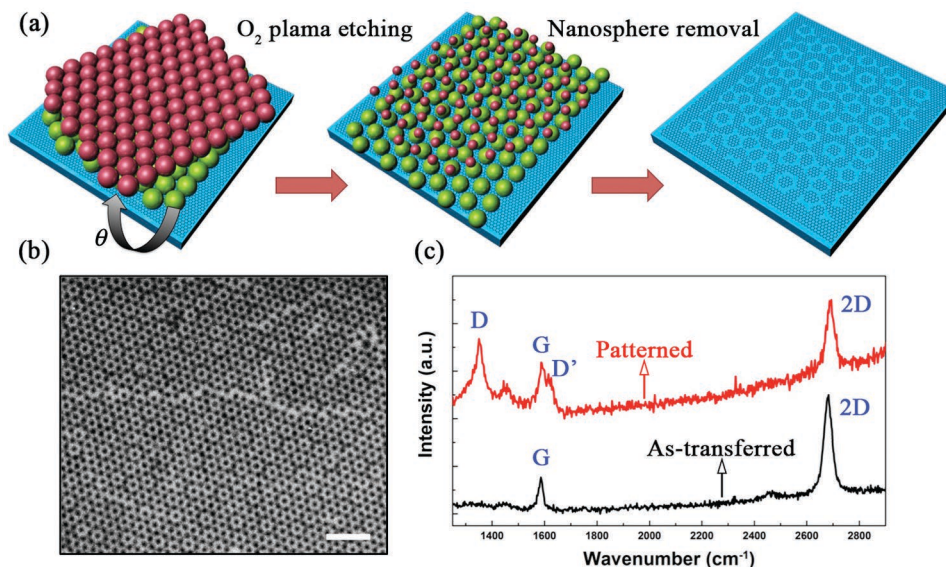


Figure 1. a) Schematics of the fabrication processes of the graphene moiré metasurfaces on Si substrates (blue). θ denotes the relative rotation angle between the bottom (green) and top (red) monolayers of polystyrene (PS) nanospheres. b) SEM image of a representative fabricated graphene moiré metasurface. The black and white areas are graphene and substrate, respectively. The scale bar is 2 μm . c) Raman spectra of as-transferred (bottom) and patterned (top) graphene samples.

the size and shape of the interstices varies significantly with the changing of the relative rotation angle. At large relative rotation angle, the interstices form moiré pattern composed of interstices with holes arrays, triangles, and z-shaped structures. When increasing the relative rotation angle, the size of unit cells and the spacing between unit cells become smaller. An even larger rotation angle will result in even more complex structures including individual, double, and triple ring-like structures, as well as triangular nanostructures, which are attributed to the larger spatial mismatch between the top and the bottom monolayers of the PS nanospheres. After the graphene exposed at the interstices between PS nanospheres is etched away by the O_2 plasma, the moiré patterns formed by the relative rotation of the two monolayers of PS nanospheres are transferred to the graphene sheets. Figure 2d–f shows the SEM images of the graphene sheets with moiré patterns fabricated with different relative rotation angles corresponding to Figure 2a–c. It can be observed that the moiré patterns in the PS nanosphere masks are perfectly transferred to the graphene sheets.

More interestingly, by slightly modifying the fabrication process, we can further extend the family of graphene moiré metasurfaces. As schematically shown in Figure S2 (Supporting Information), anti-moiré patterns on graphene sheets can be created by adding a thin layer of PMMA as a sacrificing layer. Figure 2g–i shows the SEM images of graphene sheets with anti-moiré patterns. These patterns correspond to relative rotation angle of 7.5° , 12° , and 19° between the two PS nanosphere layers, respectively. The images show more complex graphene nanoparticles, including nanotriangles, z-shaped nanostructures, and single, double, and triple nanorings. Besides shape complexity and gradient, large gradient in the feature size of graphene nanoparticles in a single metasurface is observed. As shown in Figure 2g, the edge length of the triangles is ≈ 200 nm,

while the length of the longest z-shaped is ≈ 1.1 μm . Together with the holes and shorter z-shapes structures with feature size of ≈ 500 and 625 nm, this graphene anti-moiré metasurface show large gradient in feature size from ≈ 200 nm to ≈ 1.1 μm . Similar gradient can also be observed for the interstices in graphene moiré metasurfaces with rotation angle of 7.5° , as shown in Figure 2d. Such large structural gradient in single metasurfaces is very useful for multifunctional optoelectronic devices, including biomedical sensing,^[50] tailored light modulation,^[36] and shielding technology.^[51]

The shape and size of the graphene nanostructures can be further varied and tuned via controlling the etching process and the size of the PS nanospheres applied for the fabrication. With different etching time during the O_2 RIE to reduce the size of the PS nanospheres, the shape of the voids in the PS nanosphere masks can be varied, thus resulting graphene nanostructures with controllable shapes. Figure 3a,b shows the graphene anti-moiré metasurfaces with a relative rotation angle of $\approx 19^\circ$. The graphene sheets in Figure 3a,b correspond to etching time of 100 and 140 s, respectively. The change in O_2 plasma etching time results in the difference of the interstices in the PS nanosphere masks. For shorter etching time, the interstices with ring-like structures are not completely formed, leading to split-ring structures. As a result, graphene split-ring nanostructures can be formed in the graphene anti-moiré metasurface, as shown in Figure 3a and its inset. When increasing the O_2 plasma etching time, the graphene split-ring nanostructures transfer to complete graphene ring-like nanostructures (as shown in Figure 3b and its inset), due to the complete formation of ring-like interstices in the PS nanosphere masks. The same procedure can also be applied to control the structures in graphene moiré metasurfaces. As shown in Figure 3d,e, the structures of the components in graphene moiré metasurfaces with relative rotation angle of

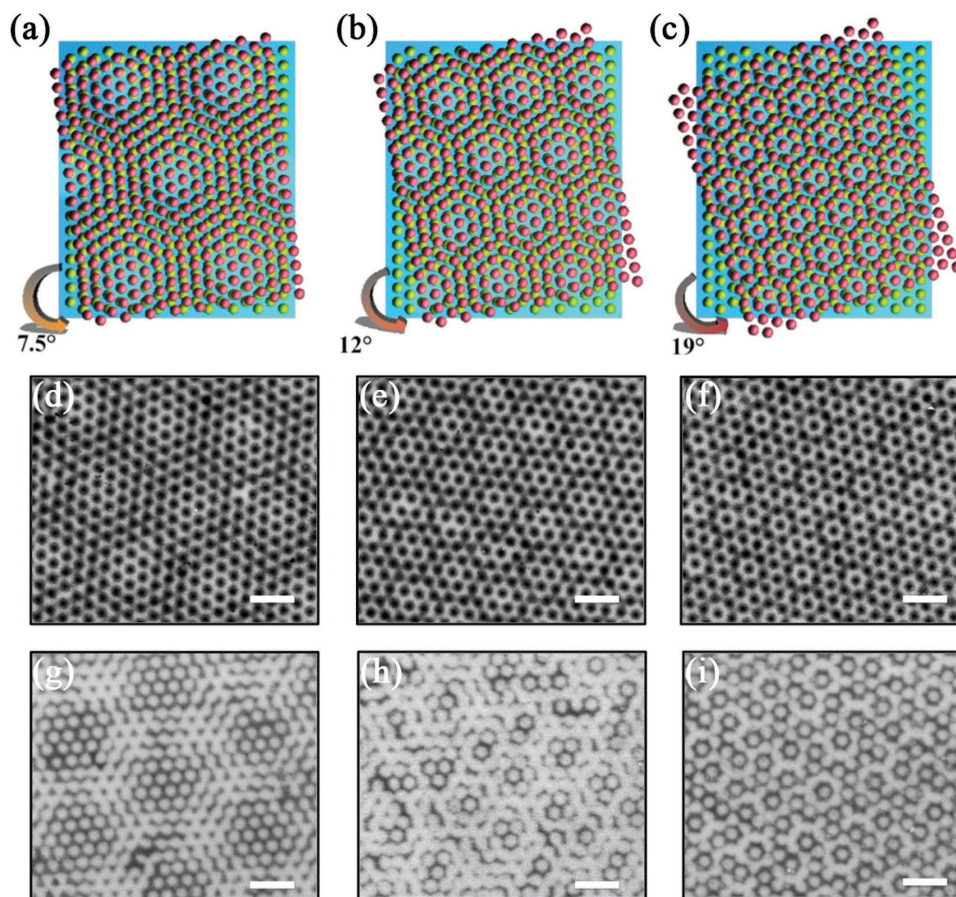


Figure 2. a–c) Schematics showing stacking of the bottom (green) and top (red) monolayers of PS nanospheres with relative in-plane rotations of a) 7.5°, b) 12°, and c) 19°, resulting in the formation of various moiré patterns. d–f) SEM images of fabricated graphene moiré metasurfaces corresponding to relative rotation of d) 7.5°, e) 12°, and f) 19°. g–i) SEM images of fabricated graphene metasurfaces with anti-moiré patterns corresponding to relative rotation of g) 7.5°, h) 12°, and i) 19° between the bottom and top monolayers of nanospheres during fabrication. The black and white areas in SEM images are graphene and substrates, respectively. The scale bars are 1.5 μm .

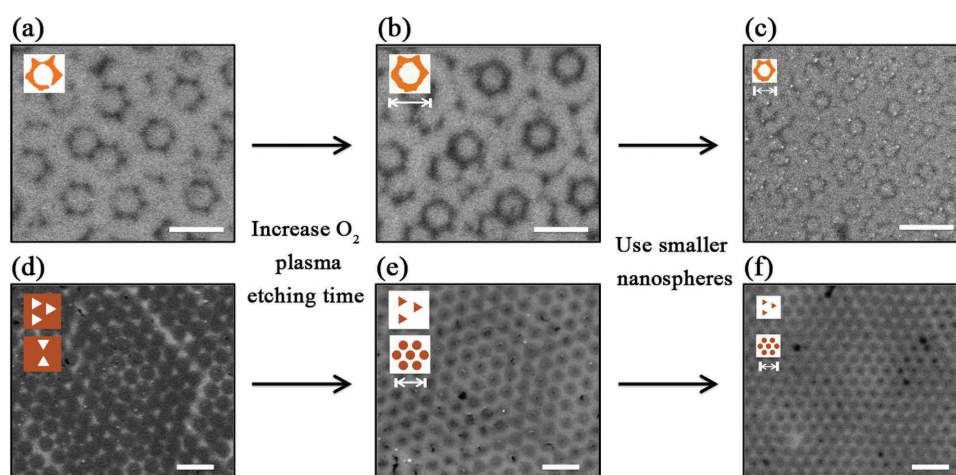


Figure 3. a–c) Graphene anti-moiré metasurfaces with the relative rotation angle of $\approx 19^\circ$. e–f) Graphene moiré metasurfaces with the relative rotation angle of $\approx 7.5^\circ$. The graphene metasurfaces in a, b, d, and e are fabricated using PS nanospheres with diameter of 500 nm, while the metasurfaces in (c) and (f) are fabricated using nanospheres with diameter of 300 nm. The black and white areas in SEM images are graphene and substrates, respectively. The scale bars are 1 μm . The insets show the representative nanostructures that undergo changes in shape or size after modifying parameters during fabrication. The dark red areas in the schematics represent graphene, while the white areas represent Si substrates that are not covered with graphene.

$\approx 7.5^\circ$ can also be tuned through changing the O_2 plasma etching time. The O_2 RIE duration for the graphene moiré metasurfaces in Figure 3d,e is 100 and 140 s, respectively. In the graphene moiré metasurfaces shown in Figure 3d, the moiré patterns is mainly composed of triangular antidot arrays and triangular antidot bowtie structures, as schematically depicted in the insets. When increasing the O_2 RIE duration, the graphene triangular antidots become larger and evolve to arrays of graphene triangles, as schematically shown by the top inset in Figure 3e. Similarly, the size of the triangular antidote bowtie structures increases with longer O_2 RIE duration, as schematically shown by the bottom inset in Figure 3e. As a result, the graphene moiré/anti-moiré metasurfaces with longer O_2 RIE duration have very different character than the one with shorter RIE duration, even though they have the same relative rotation angle. Further structural manipulations on the graphene moiré/anti-moiré metasurfaces can be achieved by changing the size of the PS nanospheres used during MNSL. As an example, we used PS nanospheres with diameter of 300 nm to repeat the fabrication. The resulting graphene metasurfaces shown in Figure 3c,f have similar patterns to those in Figure 3b,e, but the feature size of the components is proportionally reduced by 40%. Due to the use of the smaller PS spheres, the O_2 RIE duration for the graphene moiré metasurfaces in Figure 3c,f was reduced to 75 s. Since we use commercially available PS nanospheres (Thermo Scientific Inc.) for the fabrication and the available size of the PS nanospheres is ranging from 60 nm to 100 μm , we expect that we can easily control the feature size of the graphene moiré/anti-moiré metasurfaces from sub-60 nm to micrometer scale. The high tunability of both the pattern and feature size of the graphene moiré/anti-moiré metasurfaces makes our approach promising for fabricating optoelectronic devices with tunable responses.

Graphene nanostructures can support strong plasmon resonances with the resonance wavelength being a function of the shape and size of the nanostructures.^[2,11,49,52,53] Graphene moiré/anti-moiré metasurfaces can support multiple plasmon resonances due to the variety of sizes and shapes of graphene nanostructures in their composition. We characterized the optical extinction of graphene moiré/anti-moiré metasurfaces (as shown in Figure 4) with three different patterns in MIR spectral range. The graphene metasurface with pattern 1 have moiré pattern composed of graphene nanodisk arrays and triangular antidot arrays. Graphene metasurfaces with pattern 2 and 3 have anti-moiré patterns. Pattern 2 has graphene nanorings and nanotriangles, while the main components in pattern 3 are graphene nanotriangles and nanohole arrays. The spectra in Figure 4b show the transmission extinction of these three graphene moiré metasurfaces in MIR regime. The transmission extinction is calculated as $1 - T/T_0$, where T and T_0 are measured power transmission of graphene moiré/anti-moiré metasurfaces on Si substrates and pure Si substrates without graphene. It can be observed that the graphene metasurfaces

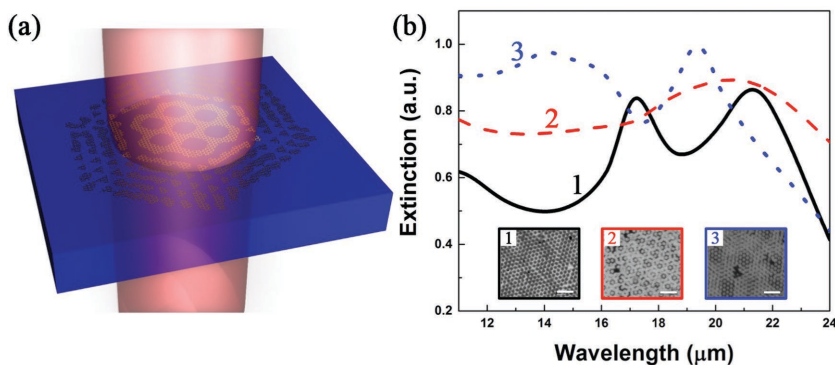


Figure 4. a) Schematic illustration of transmission extinction measurement of graphene moiré metasurfaces. The graphene nanostructures illuminated by incident light are excited to support surface plasmon resonances, resulting extinction in transmission. b) Measured extinction spectra of three graphene moiré metasurfaces with different patterns. The black and white areas in SEM images are graphene and substrates, respectively. The scale bars are 1.5 μm .

with different patterns show obvious differences in the number of peaks and the peak wavelengths.

To further understand the origins of the extinction peaks, we applied finite-difference time-domain (FDTD) method to simulate the transmission extinction of the graphene nanostructures in these three metasurfaces. The graphene is modeled as a 2D surface with surface conductivity.^[54] The black and red curves (bottom) in Figure 5a are the simulated extinction spectra of graphene disk arrays and triangular antidots, respectively, in graphene metasurface 1 in Figure 4. The experimentally measured extinction of the metasurface 1 is also shown by blue curve (top) in Figure 5a. The measured spectrum is offset vertically for clarity. It can be observed that the measured extinction peak at shorter wavelength of $\approx 17 \mu\text{m}$ match well with the simulated extinction peak (mode 1) of the triangular antidot, while the measured extinction peak at longer wavelength of $\approx 21.5 \mu\text{m}$ (mode 2) matches well with the simulated extinction peak of the graphene nanodisk. We further analyze the simulated electric field distributions of these graphene nanostructures at their extinction peak wavelength, as shown in Figure 5d,e. The simulations reveal that the dipolar plasmon resonance modes of these two nanostructures are excited at their peak resonance wavelengths. Similarly, the simulated extinction spectrum of graphene nanotriangles shows an extinction peak that is matching well with the measured extinction peak of the graphene metasurface with pattern 2 in Figure 4, as shown in Figure 5b. The electric field distribution in Figure 5f shows that the corresponding resonance of graphene nanotriangle is dominated by a dipolar mode located at the edge driven by the electric field along x direction. Our results reveal that the measured extinction peaks of the graphene moiré/anti-moiré metasurfaces are attributed to the plasmon resonances of the graphene nanostructures excited by the incident electromagnetic wave.

It is worth noting that the nanorings in the graphene metasurface with pattern 2 can also support plasmon resonances. As shown by the simulated extinction spectrum and electric-field mapping in Figure S3 (Supporting Information), the resonance wavelength of the graphene nanorings is 69 μm , which is much longer than that of the graphene nanotriangles and far beyond the working wavelengths of the mid-infrared detector

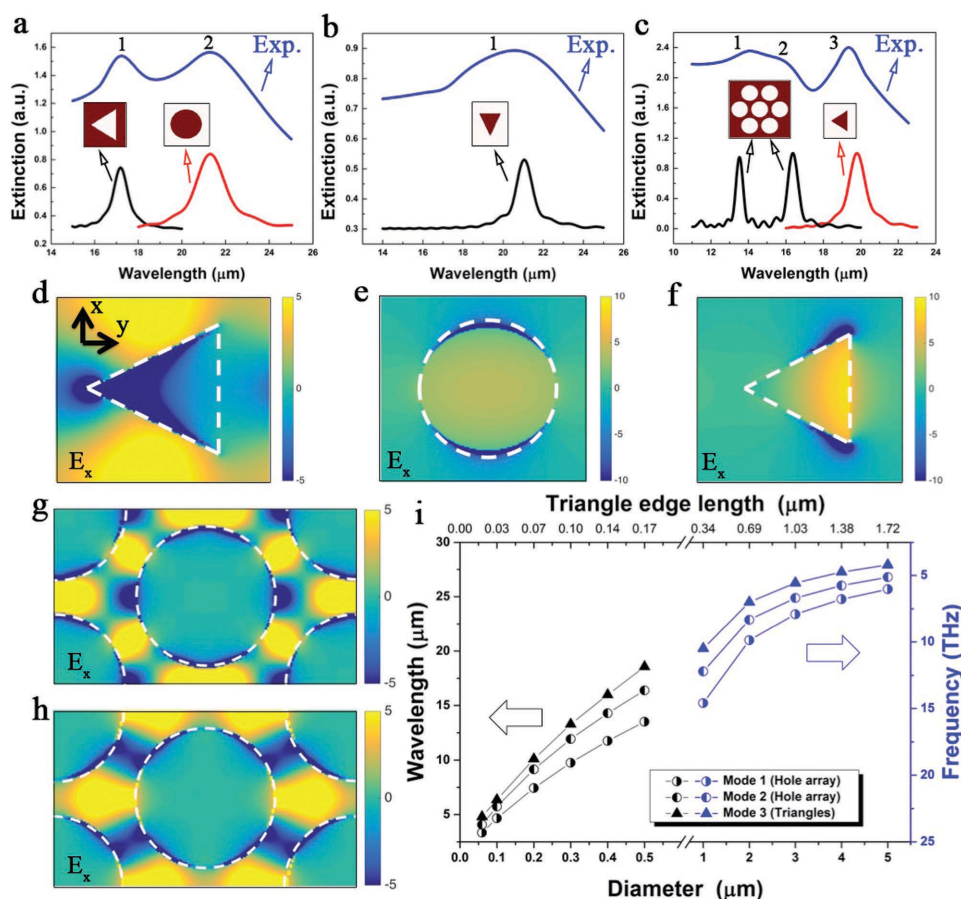


Figure 5. a–c) Measured extinction spectra of graphene moiré/anti-moiré metasurfaces with pattern 1a), pattern 2b), and pattern 3c) in Figure 4. The small numbers above the spectra depict the corresponding modes. Simulated extinction spectra for different components (shown by the schematics) in the corresponding graphene metasurfaces are also shown below the measured spectra to demonstrate the origins of the peaks in the measured extinction spectra. d–f) Simulated electric field mapping at the resonances wavelength of graphene d) triangular antidot, e) disk, and f) triangle, respectively. g, h) Simulated electric field mapping of g) mode 1 and h) mode 2 of graphene hole array, respectively. The polarizations of the incident electromagnetic wave are along the x direction as depicted in (d). i) Dependence of simulated extinction peak positions of graphene metasurface with pattern 3 on the diameter of original PS nanospheres and the resulted edge length of graphene nanotriangles. The peak wavelength and frequency are used for the extinction spectra from the small and large diameters of PS spheres, respectively.

in our current spectrometer. More interestingly, as shown in Figure 5c, the simulated extinction spectrum of the graphene nanohole array shows two extinction peaks, which have a good match with the two shorter extinction peaks (mode 1 and 2) in the measured spectrum. The electric field distributions of the graphene nanohole array at the wavelengths of these two modes are shown in Figure 5g, h, respectively. It can be observed that two different plasmon resonance modes are excited at these two wavelengths. In combined with the plasmon resonance modes supported by the graphene nanotriangles, as revealed by Figure 5c, three extinction peaks can be observed between 10 and 20 μm for single graphene anti-moiré metasurface with pattern 3. Our results demonstrate the unique capability of graphene moiré/anti-moiré metasurfaces to achieve tunable optical responses with controllable number of working bands in a wide range of wavelength regime.

Compared with pristine graphene, graphene nanostructures in moiré/anti-moiré metasurfaces exhibit much stronger interactions with incident light at the plasmon resonances. In Figure S4a–c, no near-field enhancement can be observed

for pristine graphene at the plasmon resonance wavelengths of graphene triangular antidot, triangle, and disk as shown in Figure 5d–f. In Figure S4d, a comparison of extinction spectra of the pristine graphene and the three graphene nanostructures further confirms that the weak light-matter interaction at the pristine graphene is correlated with the lack of plasmon resonances. The strong light-matter interaction and near-field enhancement at the patterned graphene is significant for many applications. One example is the use of graphene nanostructures for SEIRS. It has been widely reported that the enhancement factor of SEIRS is proportional to E^2 , where E is the electric field at the location of molecules near the plasmonic structures.^[55] Another example is surface-enhanced light emission, where the spontaneous emission rate of an emitter can be strongly enhanced by confined electric field at plasmon resonances.^[56,57] Thus, patterning of graphene into moiré patterns with sub-wavelength features can enhance the light-matter interactions at multiple wavelengths due to the excitation of plasmon resonances, which can benefit a variety of applications, including sensing, light modulation, and light emission enhancement.

For graphene nanostructures, taking graphene disk as an example, the extinction in transmission is given by^[2]

$$1 - T/T_0 = 1 - \frac{1}{|1 + Z_0 \sigma(\omega)/(1 + n_s)|^2} \quad (1)$$

where Z_0 is the vacuum impedance, $\sigma(\omega)$ is the frequency (ω)-dependent conductivity, and n_s is the refractive index of the substrate. Neglecting the lateral nanostructure interaction, the optical conductivity can be represented by^[58]

$$\sigma(\omega) \propto \frac{\omega}{(\omega^2 - \omega_p^2) + i\Gamma_p \omega} \quad (2)$$

where the ω_p and Γ_p are plasmon resonance frequency and plasmon resonance width. The resonance frequency can be further given by^[2]

$$\omega_p = \sqrt{\frac{3D}{8\epsilon_m \epsilon_0 d}} \quad (3)$$

where D , ϵ_m , ϵ_0 , and d are the Drude weight, media dielectric constant, vacuum permittivity, and the diameter of the graphene disk. As a result, the extinction peak of graphene nanodisks is highly dependent on their size. As discussed in Figure 3, the feature size of the graphene moiré/anti-moiré metasurfaces can be tuned from sub-60 nm to micrometer scale while maintaining the patterns, simply by selecting the size of commercially available PS nanospheres applied for MNSL. Based on the above analysis, we expect that the extinction peaks of the graphene moiré/anti-moiré metasurfaces can be flexibly tuned by changing the size of the PS nanospheres applied for MNSL. Figure 5i shows the simulated positions of the three extinction peaks of the anti-moiré metasurfaces (pattern 3 in Figure 4) versus the original diameters of the PS nanospheres. In principle, for each original size of the PS spheres, there can be a series of metasurfaces where the sizes of holes and triangles can be continuously tuned via controlling the etching process. Our data in Figure 5i compare those metasurfaces with the same specified ratio of hole diameter and triangle edge length. Specifically, we start with the metasurface model based on the experimental parameters in pattern 3 of Figure 4, where the hole diameter and the edge length of the nanotriangle are ≈ 400 and ≈ 170 nm, respectively, and the original diameter of PS sphere is 500 nm. Therefore, the ratio between the hole diameter and the diameter of the nanospheres is 1.25, and the ratio between the triangle edge length and the diameter of the nanospheres is 2.94. For other metasurfaces from different original diameters of PS spheres, we linearly scale the metasurface model for pattern 3 in Figure 4 to retain the same ratios, which can be achieved by controlling the O_2 plasma etching in experiment. We can see that the three extinction peaks can be tuned across a wide wavelength range from ≈ 5 μm to ≈ 60 μm . The 60 μm corresponds to 5 THz in frequency in Figure 5i. Compared with the relatively narrow tunable range (≈ 20 μm) through controlling the Fermi level (as shown in Figure S5, Supporting Information), a much larger tunability of about 60 μm can be achieved for all the three extinction peaks in single graphene anti-moiré metasurfaces. Due to the

high repeatability of fabrication by our proposed methods, and the capability of nanosphere lithography towards large area (≈ 1 m^2) and high throughput (2500–3000 wafers h^{-1}) fabrication,^[59] these graphene metasurfaces are highly promising for practical multiband optoelectronic devices requiring a wide tunability on working bands.

3. Conclusion

In summary, we have demonstrated large-area fabrication of graphene moiré and anti-moiré metasurfaces by cost-effective self-assembly-based MNSL. The moiré/anti-moiré patterns with large structural gradient can be easily tuned by varying the relative rotation angle between the top and bottom monolayers of PS nanospheres. Extra freedom on the structural tunability can be introduced by controlling the etching time of PS nanospheres and the original size of PS nanospheres in MNSL. More complex graphene metasurfaces can be achieved by incorporating angle-variable nanosphere etching and metal deposition. Our experimental and numerical studies reveal that the extinction spectra of the graphene metasurfaces are controllable through tuning the patterns, due to the size and shape dependence of the surface plasmon resonances of the graphene nanostructures. Multiband graphene metasurfaces are achieved in a wide range of working wavelengths from the complex and gradient nanostructures in moiré patterns.

With the tunable and multiple plasmon resonance modes in a wide range of electromagnetic spectra from MIR to THz, graphene moiré/anti-moiré metasurfaces can be promising candidates for frequency-selective surfaces, ultrathin light modulators, biosensors, and photodetectors with multispectral responses. Such patterned graphene arrays may also find applications in magneto-optics. Recently, Hadad et al. proposed a paradigm of graphene metaatoms and metasurfaces to overcome the constraint of high magnetic field for induction of optical response in graphene.^[6] Specifically, hexagonal periodic arrays of metaatoms consisted of small circular regions with a conductivity different from that in the rest of the graphene sheet have been demonstrated to exhibit unprecedentedly strong magneto-optical activity at low magnetization. With the rotation symmetry and quasiperiodicity, graphene metasurfaces with moiré patterns may induce strong magneto-optical activity at multiple resonances, enabling advanced applications in nonreciprocal photonics.

4. Experimental Section

Growth and Transfer of Large Area Graphene: Copper foils (35 μm thick, Miller-Cu, Mitsui Mining and Smelting Co. Ltd.) were used as the catalytic substrates. The substrates were loaded into a quartz tubular furnace and the air was evacuated. The vacuum was then purged with Ar/ H_2 gas mixture (Ar at 300 sccm and H_2 at 10 sccm) to restore pressure to atmospheric, followed by ramping up the furnace temperature to 1030 $^\circ\text{C}$. Once the temperature was reached, it was held for 15 min for annealing. After annealing finished, the gas flow rate was changed (Ar at 500 sccm, H_2 at 75 sccm, and CH_4 at 2 sccm) and graphene was grown for 10 min. The samples were then cooled under the same gas flow to room temperature.

Graphene grown on Cu foil was transferred to a undoped, double-side polished Si substrate by selective etching of Cu foil using an ammonium persulfate ((NH₄)₂S₂O₈) aqueous solution. A 200 nm thick PMMA film ($M_w \approx 495\,000$ from Sigma-Aldrich) was used as a temporary support layer for transferring the graphene to a Si substrate.

Raman and Fourier Transform Infrared Spectrometer (FTIR) Characterizations: Raman spectroscopy measurements were taken with a Renishaw inVia micro-Raman system with an excitation wavelength of 532 nm and a grating of 1200 lines mm⁻¹.

We measured the transmission spectra using a FTIR operating in a step-scan mode. The unpolarized broadband infrared light from a thermal Globar source of the FTIR was modulated by an optical chopper at the frequency of 500 Hz and focused onto the sample surface using a reflective objective. The transmitted signal collimated by two ZnSe lenses was collected and averaged by a mid-infrared HgCdTe detector and lock-in-amplifier, respectively.

Numerical Simulations: The simulations of the extinction spectra and electric field distributions were conducted using FDTD methods with commercially available software package (FDTD Solutions, Lumerical). The graphene moiré metasurfaces were positioned on top of a Si substrate with a 2 nm native SiO₂ oxidation layer. The graphene was modeled as a surface conductivity material. A chemical potential of 0.6 eV was used during simulations. This value was estimated in the consideration of doping of graphene during the O₂ plasma process.¹⁶⁰ The SiO₂ and Si were modeled as dielectric materials with refractive index of 1.4 and 3.42, respectively. Normal incident plane waves were used as light sources. 2D frequency domain power and field detectors were used to obtain the transmittance through the graphene moiré metasurfaces and the electric field distributions.

Supporting Information

Supporting Information is available from the Wiley Online Library or from the author.

Acknowledgements

Z.W. and W.L. contributed equally to this work. The authors acknowledge the financial support of the Beckman Young Investigator Program (Y.Z.), a Multidisciplinary University Research Initiative from the Air Force Office of Scientific Research (AFOSR MURI Award No. FA9550-12-1-0488) (S.B.), and the Texas Advanced Computing Center (TACC) at The University of Texas at Austin for providing high performance computing (HPC) resources that have contributed to numerical simulations. URL: <http://www.tacc.utexas.edu>. M.A.B. acknowledges support from the Welch Foundation Grant No. F-1705. The authors thank J. Wozniak for improving the figures in the paper.

Received: April 5, 2016
Revised: June 24, 2016
Published online:

- [1] F. Xia, H. Wang, D. Xiao, M. Dubey, A. Ramasubramaniam, *Nat. Photonics* **2014**, *8*, 899.
- [2] H. Yan, X. Li, B. Chandra, G. Tulevski, Y. Wu, M. Freitag, W. Zhu, P. Avouris, F. Xia, *Nat. Nanotechnol.* **2012**, *7*, 330.
- [3] L. Yan, Y. B. Zheng, F. Zhao, S. Li, X. Gao, B. Xu, P. S. Weiss, Y. Zhao, *Chem. Soc. Rev.* **2012**, *41*, 97.
- [4] S. Rahimi, L. Tao, S. F. Chowdhury, S. Park, A. Jouvray, S. Buttress, N. Rupasinghe, K. Teo, D. Akinwande, *ACS Nano* **2014**, *8*, 10471.
- [5] Z. Shi, R. Yang, L. Zhang, Y. Wang, D. Liu, D. Shi, E. Wang, G. Zhang, *Adv. Mater.* **2011**, *23*, 3061.
- [6] Y. Hadad, A. R. Davoyan, N. Engheta, B. Z. Steinberg, *ACS Photonics* **2014**, *1*, 1068.
- [7] Y. Hadad, A. R. Davoyan, N. Engheta, B. Z. Steinberg, in *2014 Int. Conf. Electromagnetics Advanced Applications (ICEAA)*, IEEE, Piscataway, NJ, USA **2014**, DOI: 10.1109/ICEAA.2014.6903937.
- [8] Y. Hadad, B. Z. Steinberg, A. Davoyan, N. Engheta, in *2014 IEEE Antennas Propagation Society Int. Symp. (APSURSI)*, IEEE, Piscataway, NJ, USA **2014**, DOI: 10.1109/APS.2014.6904343.
- [9] T. Low, P. Avouris, *ACS Nano* **2014**, *8*, 1086.
- [10] V. W. Brar, M. C. Sherrott, M. S. Jang, S. Kim, L. Kim, M. Choi, L. A. Sweatlock, H. A. Atwater, *Nat. Commun.* **2015**, *6*, 7032.
- [11] D. B. Farmer, D. Rodrigo, T. Low, P. Avouris, *Nano Lett.* **2015**, *15*, 2582.
- [12] X. Cai, A. B. Sushkov, M. M. Jadidi, L. O. Nyakiti, R. L. Myers-Ward, D. K. Gaskill, T. E. Murphy, M. S. Fuhrer, H. D. Drew, *Nano Lett.* **2015**, *15*, 4295.
- [13] I. Silveiro, J. M. P. Ortega, F. J. G. de Abajo, *Light: Sci. Appl.* **2015**, *4*, e241.
- [14] Z. Q. Li, E. A. Henriksen, Z. Jiang, Z. Hao, M. C. Martin, P. Kim, H. L. Stormer, D. N. Basov, *Nat. Phys.* **2008**, *4*, 532.
- [15] D. Jin, A. Kumar, K. H. Fung, J. Xu, N. X. Fang, *Appl. Phys. Lett.* **2013**, *102*, 201118.
- [16] Z. Li, K. Yao, F. Xia, S. Shen, J. Tian, Y. Liu, *Sci. Rep.* **2015**, *5*, 12423.
- [17] D. Rodrigo, O. Limaj, D. Janner, D. Etezadi, F. J. G. de Abajo, V. Pruneri, H. Altug, *Science* **2015**, *349*, 165.
- [18] A. Marini, I. Silveiro, F. J. G. de Abajo, *ACS Photonics* **2015**, *2*, 876.
- [19] B. Sensale-Rodriguez, R. Yan, M. M. Kelly, T. Fang, K. Tahy, W. S. Hwang, D. Jena, L. Liu, H. G. Xing, *Nat. Commun.* **2012**, *3*, 780.
- [20] M. Mehmood, S. Mei, S. Hussain, K. Huang, S. Siew, L. Zhang, T. Zhang, X. Ling, H. Liu, J. Teng, A. Danner, S. Zhang, C.-W. Qiu, *Adv. Mater.* **2016**, *28*, 2533.
- [21] L. Zhang, S. Mei, K. Huang, C.-W. Qiu, *Adv. Opt. Mater.* **2016**, *4*, 818.
- [22] A. B. Khanikaev, N. Arju, Z. Fan, D. Purtseladze, F. Lu, J. Lee, P. Sarriugarte, M. Schnell, R. Hillenbrand, M. A. Belkin, G. Shvets, *Nat. Commun.* **2016**, *7*, 12045.
- [23] X. Liu, T. Starr, A. F. Starr, W. J. Padilla, *Phys. Rev. Lett.* **2010**, *104*, 207403.
- [24] Z. Wu, K. Chen, R. Menz, T. Nagao, Y. Zheng, *Nanoscale* **2015**, *7*, 20391.
- [25] C. D'Andrea, J. Bochterle, A. Toma, C. Huck, F. Neubrech, E. Messina, B. Fazio, O. M. Maragò, E. Di Fabrizio, M. L. de La Chapelle, P. G. Gucciardi, A. Pucci, *ACS Nano* **2013**, *7*, 3522.
- [26] K. Chen, R. Adato, H. Altug, *ACS Nano* **2012**, *6*, 7998.
- [27] H. Aouani, H. Šípová, M. Rahmani, M. Navarro-Cia, K. Hegnerová, J. Homola, M. Hong, S. A. Maier, *ACS Nano* **2013**, *7*, 669.
- [28] L. Cao, M. L. Brongersma, *Nat. Photonics* **2009**, *3*, 12.
- [29] J. Lee, M. Tymchenko, C. Argyropoulos, P.-Y. Chen, F. Lu, F. Demmerle, G. Boehm, M.-C. Amann, A. Alu, M. A. Belkin, *Nature* **2014**, *511*, 65.
- [30] C. D'Andrea, J. r. Bochterle, A. Toma, C. Huck, F. Neubrech, E. Messina, B. Fazio, O. M. Marago, E. Di Fabrizio, M. L. de La Chapelle, *ACS Nano* **2013**, *7*, 3522.
- [31] C. Xu, F. Wen-Hui, *Mater. Res. Express* **2015**, *2*, 055801.
- [32] F. Laghezza, F. Scotti, G. Serafino, S. Pinna, D. Onori, E. Lazzari, P. Ghelfi, A. Bogoni, in *2015 14th Int. Conf. Optical Communication Networks (ICOCN)*, IEEE, Piscataway, NJ, USA **2015**, DOI: 10.1109/ICOCN.2015.7203731.
- [33] Y.-F. Lao, G. Ariyawansa, A. G. Unil Perera, *J. Appl. Phys.* **2011**, *110*, 043112.
- [34] S. Gottheim, H. Zhang, A. O. Govorov, N. J. Halas, *ACS Nano* **2015**, *9*, 3284.

- [35] S. M. Lubin, A. J. Hryn, M. D. Huntington, C. J. Engel, T. W. Odom, *ACS Nano* **2013**, *7*, 11035.
- [36] J. Zhao, S. Jaber, P. Mulvaney, P. V. Braun, H. Giessen, *Adv. Opt. Mater.* **2015**, *3*, 680.
- [37] T. Matsui, A. Agrawal, A. Nahata, Z. V. Vardeny, *Nature* **2007**, *446*, 517.
- [38] K. Chen, B. B. Rajeeva, Z. Wu, M. Rukavina, T. D. Dao, S. Ishii, M. Aono, T. Nagao, Y. Zheng, *ACS Nano* **2015**, *9*, 6031.
- [39] S. Qiao, Y. Zhang, S. Liang, L. Sun, H. Sun, G. Xu, Y. Zhao, Z. Yang, *J. Appl. Phys.* **2015**, *118*, 123106.
- [40] Z. Shi, C. Jin, W. Yang, L. Ju, J. Horng, X. Lu, H. A. Bechtel, M. C. Martin, D. Fu, J. Wu, K. Watanabe, T. Taniguchi, Y. Zhang, X. Bai, E. Wang, G. Zhang, F. Wang, *Nat. Phys.* **2014**, *10*, 743.
- [41] G. X. Ni, H. Wang, J. S. Wu, Z. Fei, M. D. Goldflam, F. Keilmann, B. Ozyilmaz, A. H. Castro Neto, X. M. Xie, M. M. Fogler, D. N. Basov, *Nat. Mater.* **2015**, *14*, 1217.
- [42] G. T. de Laissardière, D. Mayou, L. Magaud, *Nano Lett.* **2010**, *10*, 804.
- [43] K. Zhang, L. Zhang, F. L. Yap, P. Song, C. W. Qiu, K. P. Loh, *Small* **2016**, *12*, 1302.
- [44] Z. Huang, H. Fang, J. Zhu, *Adv. Mater.* **2007**, *19*, 744.
- [45] A. L. Lee, L. Tao, D. Akinwande, *ACS Appl. Mater. Interfaces* **2015**, *7*, 1527.
- [46] J. Lee, T.-J. Ha, H. Li, K. N. Parrish, M. Holt, A. Dodabalapur, R. S. Ruoff, D. Akinwande, *ACS Nano* **2013**, *7*, 7744.
- [47] A. Eckmann, A. Felten, A. Mishchenko, L. Britnell, R. Krupke, K. S. Novoselov, C. Casiraghi, *Nano Lett.* **2012**, *12*, 3925.
- [48] A. C. Ferrari, D. M. Basko, *Nat. Nanotechnol.* **2013**, *8*, 235.
- [49] X. Zhu, W. Wang, W. Yan, M. B. Larsen, P. Boggild, T. G. Pedersen, S. Xiao, J. Zi, N. A. Mortensen, *Nano Lett.* **2014**, *14*, 2907.
- [50] N. Zhang, K. Liu, Z. Liu, H. Song, X. Zeng, D. Ji, A. Cheney, S. Jiang, Q. Gan, *Adv. Mater. Interfaces* **2015**, *2*, 1500142.
- [51] G.-H. Yang, X.-X. Liu, Y.-L. Lv, J.-H. Fu, Q. Wu, X. Gu, *J. Appl. Phys.* **2014**, *115*, 17E523.
- [52] Z. Fang, S. Thongrattanasiri, A. Schlather, Z. Liu, L. Ma, Y. Wang, P. M. Ajayan, P. Nordlander, N. J. Halas, F. J. G. de Abajo, *ACS Nano* **2013**, *7*, 2388.
- [53] W. Wang, T. Christensen, A. P. Jauho, K. S. Thygesen, M. Wubs, N. A. Mortensen, *Sci. Rep.* **2015**, *5*, 9535.
- [54] G. W. Hanson, *J. Appl. Phys.* **2008**, *103*, 064302.
- [55] F. Le, D. W. Brandl, Y. A. Urzhumov, H. Wang, J. Kundu, N. J. Halas, J. Aizpurua, P. Nordlander, *ACS Nano* **2008**, *2*, 707.
- [56] Z. Wu, Y. Zheng, *Plasmonics* **2015**, *11*, 1.
- [57] G. M. Akselrod, C. Argyropoulos, T. B. Hoang, C. Ciraci, C. Fang, J. Huang, D. R. Smith, M. H. Mikkelsen, *Nat. Photonics* **2014**, *8*, 835.
- [58] S. Thongrattanasiri, F. H. L. Koppens, F. J. G. de Abajo, *Phys. Rev. Lett.* **2012**, *108*, 047401.
- [59] P. Gao, J. He, S. Zhou, X. Yang, S. Li, J. Sheng, D. Wang, T. Yu, J. Ye, Y. Cui, *Nano Lett.* **2015**, *15*, 4591.
- [60] K. Y. Yeung, J. Chee, Y. Song, J. Kong, D. Ham, *Nano Lett.* **2015**, *15*, 5001.